Full length article

First-principles investigation of the trivacancy capture cross-section in silicon

Vladislav Pelenitsyn [a,b,*], Pavel Korotaev [a]

[a] *Dukhov Automatics Research Institute (VNIIA), 22, Sushchevskaya str, Moscow, 127055, Russia*
[b] *Moscow Institute of Physics and Technology, 9 Institutsky lane, Dolgoprudny, 141700, Russia*

ARTICLE INFO

ABSTRACT

The investigation of defect properties in silicon, including charge transition levels and non-radiative carrier capture, has been ongoing for over 60 years. However, many questions still lack a complete understanding. Bistable defects are of particular interest due to their ability to have different atomic configurations. Our focus is on the bistable trivacancy in silicon. This study reports on the atomic configurations, formation energies, charge transition levels, and carrier capture cross-sections. The results were obtained through first-principles density-functional calculations using a hybrid exchange–correlation energy functional. To calculate capture cross-sections, a one-dimensional approximation is used for the configurational coordinate diagrams, taking into account anharmonicity and a static approximation for calculating the matrix elements of electron–phonon interaction. The resulting atomic structures and charge transition levels are in excellent agreement with previous experimental and theoretical studies. The obtained hole capture cross-sections by donor levels agree with experimental apparent values. The electron capture cross-sections are approximately two orders of magnitude lower than experimental values. This discrepancy can be explained by the use of the one-dimensional approximation. The cross-section values obtained made it possible to estimate the generation current at $T = 300$ K and to demonstrate that the acceptor level $\varepsilon(0/1-)$ of the "part of the hexagonal ring" (PHR) configuration is the effective recombination center responsible for the generation current in the reverse biased silicon diode under irradiation.

1. Introduction

Over the past few decades, much attention has been devoted to secondary defects in silicon, which are formed through the interaction of intrinsic defects and impurities with radiation damage products including vacancies and interstitials (Frenkel defects) [1]. Defects with features such as meta- and bistability of atomic configurations are of particular interest [2,3]. A metastable defect in the same charge state may have different atomic configurations corresponding to local energy minima near the ground state. The energy difference between the ground and secondary minima is substantial ($\Delta E > kT$), leading to the irreversibility of the transition from the metastable state to the ground state. On the contrary, a bistable defect have energy minima that are close ($\Delta E \sim kT$), and under certain conditions, it can reversibly transform from one state to another. To be specific, a bistable defect can reversibly change its atomic and electronic configuration.

Different charge states of a bistable defect may correspond to different configuration states. The possibility arises to control the configuration state by changing its charge state. But this requires a detailed understanding of the atomic and electronic structures of bistable defects. Although significant progress has been achieved in identifying bistable defects through the use of electron paramagnetic resonance spectroscopy (EPR), deep-level transient spectroscopy (DLTS), infrared spectroscopy and several other techniques, some problems still remain [4–12].

To complement experiments it is useful to utilize first-principles methods such as density functional theory (DFT) for calculating defect properties. An example of the successful use of the DFT is the prediction of the bistability of a trivacancy (V_3), one of the prevalent defects in silicon irradiated with high-energy particles [13]. For many years, it was believed that the minimum energy state of V_3 corresponds to a C_{2v} symmetry configuration with three vacancies, the centers of which are sequentially arranged in a chain of Si atoms [14]. This configuration belongs to the "part of the hexagonal ring" (PHR) structures for the V_n complex ($3 \leq n \leq 5$), in which n initial atoms are sequentially removed from the hexagonal ring in the Si lattice. However, Makhov and Lewis, using DFT, reported in Ref. [13] that a more energetically favorable "fourfold-coordinated" (FFC) structures may exist for V_n. In this structures one, two, or three silicon atoms for V_5, V_4, and V_3, respectively, are located in the interstitial position between pairs of

---

* Corresponding author at: Dukhov Automatics Research Institute (VNIIA), 22, Sushchevskaya str, Moscow, 127055, Russia.
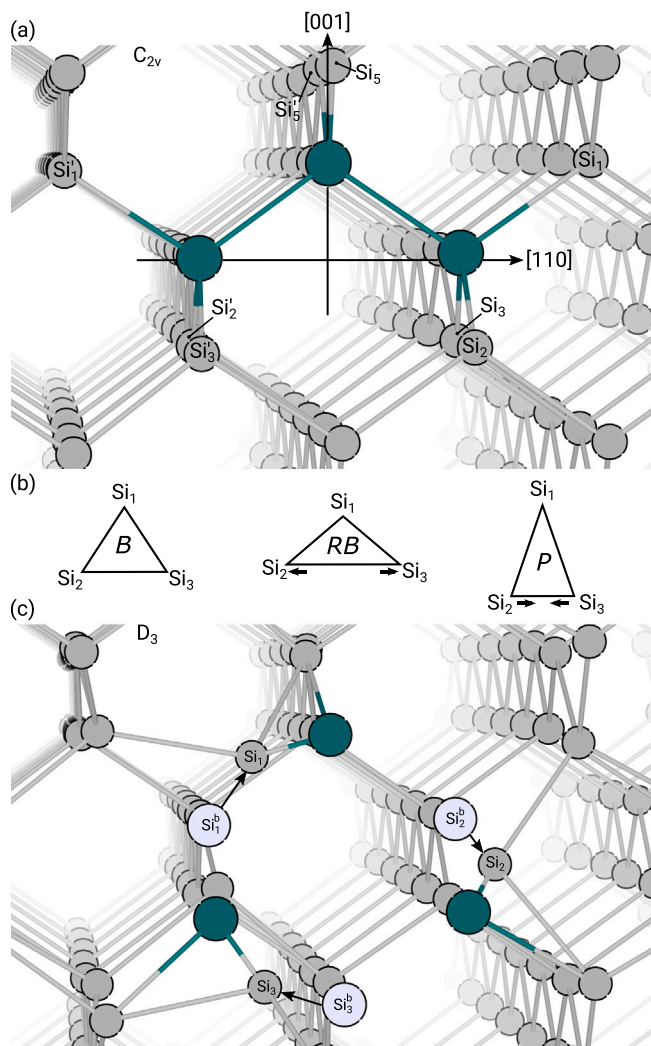*E-mail address:* pelenitsyn.vladislav@gmail.com (V. Pelenitsyn).

Fig. 1. (a) The atomic structure of $V_{3,PHR}$; (b) Possible configurations of a silicon trimer in $V_{3,PHR}$: breathing mode (B), resonant bond (RB), pairing (P) configurations; (c) The atomic structure of $V_{3,FFC}$. Silicon and vacancies are depicted by gray and green spheres, respectively. Blue spheres in (c) represent the positions of silicon atoms, Si_i, in a perfect silicon lattice, Si_i^b.

vacancies in the hexagonal ring of the V_6 complex. The PHR and FFC configurations of V_3 in Si are presented in Fig. 1.

Recently, in the series of combined DLTS and DFT studies [15–20], it has been demonstrated that V_3 is indeed a bistable defect. It was found that V_3 is in the PHR configuration immediately after irradiation of silicon. After keeping the samples for several weeks at room temperature or short annealing in the temperature range of 50–100 °C leads to the transformation of the PHR configuration into the more energetically favorable FFC configuration. Furthermore, the PHR configuration can be fully restored by applying forward bias with a current density in the range 10–25 A/cm^2. Otherwise, the FFC configuration is energetically favorable only for the neutral charge state, while the PHR configuration is favored for charged states. The charge transition levels for $V_{3,PHR}$ and $V_{3,FFC}$ calculated in these studies using the marker method are close to experimental ones.

The marker method is semi-empirical, and it is not always possible to find a defect with a similar electronic structure as a marker [21,22]. The reason for its application is the relatively simple reduction of the impact of typical errors arising in DFT calculations of formation energies and transition levels [23].

Typical errors include the energetic contribution to the formation energy from the interaction of the defect with its periodic images due to

the use of a finite size cell with periodic boundary conditions. Also, the use of traditional approximations to the exchange–correlation energy functional, such as the Local Density Approximation (LDA) or the Generalized Gradient Approximation (GGA), leads to an underestimation of a bandgap, not allowing a correct determination of the position of the defect levels relative to the band edges [24,25]. However, with increased computer performance, more accurate methods such as hybrid functionals or the GW approximation can be applied, avoiding the use of the marker method.

The aim of our work is to complement previous studies [13–20] of the bistable complex V_3 in Si with first-principles DFT calculations using the hybrid functional. Additionally, we will provide calculations of the capture cross-sections, including values that are currently experimentally unknown. The article is structured as follows: in Section 2 we provide details of the calculation methods, Section 3.1 presents the results of the investigation of the atomic structures of $V_{3,FFC}$ and $V_{3,PHR}$, Section 3.2 describes their electronic structure, Section 3.3 presents the calculated formation energies and charge transition levels, Section 3.4 presents the calculated capture cross-sections along with the discussion of the influence of V_3 on the generation current in silicon diodes. Finally, we provide a conclusion in Section 4.

2. Theoretical and computational methods

We perform calculations using the density functional theory implemented in the VASP code (version 5.4.4) [26,27]. The HSE06 hybrid functional is used, which includes 25% Hartree–Fock exchange with the screening parameter $\mu = 0.2$ Å^{-1} [28–30]. The plane-wave basis set cutoff energy was set to 450 eV to ensure energy convergence. The spin degree of freedom was also taken into account in the calculations. The silicon lattice parameter used in the calculations is $a_0 = 5.437$ Å. It was obtained from the relaxation of an 8-atom silicon primitive cell, and it is in excellent agreement with the experimental value $a_0^{exp} = 5.431$ Å [31]. The calculated bandgap $\varepsilon_g = 1.16$ eV also agree well with the experimental value at zero temperature $\varepsilon_g^{exp} = 1.17$ eV [32].

The defect was modeled using a supercell approach with a 512-atom cubic silicon supercell. The Brillouin zone was sampled at the Γ point. Relaxation of a supercell with a defect using HSE06 functional was conducted in 3 stages due to the high computational cost. In the first stage, the silicon atoms were slightly displaced to lift the system from a local minimum of high symmetry. The system was then relaxed using the PBE functional [33] and a $3 \times 3 \times 3$ Γ-centered k-points mesh. Using a denser k-points mesh results in a change in the total energy of the defective supercell of less than 1 meV, and in the average force acting on the atoms of less than 0.1 meV/Å (see Fig. S1 in the supplementary material). In the next step, the resulting structure was further relaxed using the HSE06 and the Γ point only.

The defect formation energy in charge state q was calculated as follows [34,35]:

$$E_f^q(\varepsilon_F) = E_d^q - E_{bulk} - \sum_i n_i \mu_i + q(\varepsilon_F + \varepsilon_v) + E_{corr}^q, \quad (1)$$

where E_d^q is the energy of the supercell with the defect in charge state q (which refers to the number of electrons added or removed from the supercell), E_{bulk} is the energy of the perfect supercell of the same size. The value n_i indicates the number of removed ($n_i < 0$) or added ($n_i > 0$) atoms of type i in the defective supercell, and μ_i corresponds to the chemical potential of these atoms. The Fermi level ε_F is given with respect to the valence band maximum ε_v (VBM). In systems with a net charge in the unit cell, the electrostatic energy diverges [36,37]. To eliminate this divergence, a common approach is to include a compensating homogeneous background. The correlation term E_{corr}^q takes into account the unphysical electrostatic interaction of the defect with the background, as well as the interaction with its periodic image due to periodic boundary conditions. E_{corr}^q was calculated using the scheme

proposed by Freysoldt, Neugebauer, and Van de Walle [38,39] with an experimental value of the silicon dielectric constant $\varepsilon = 11.7$ [40].

The thermodynamic charge transition level $\varepsilon(q_1/q_2)$ is the Fermi level above which the state q_2 is energetically favorable, and below which q_1 is favorable. From Eq. (1) with respect it is determined as follows:

$$\varepsilon(q_1/q_2) = \frac{E_f^{q_1}(\varepsilon_F = 0) - E_f^{q_2}(\varepsilon_F = 0)}{q_2 - q_1}. \tag{2}$$

The methodology presented, except for defect structure relaxation with the HSE06 functional, was utilized in our previous work for defects in silicon [41]. The transition level positions obtained in this manner are in excellent agreement with experimental data.

We employed the static approximation to non-radiative transitions and one-dimensional (1D) configurational diagrams considering anharmonicity for calculating capture cross-sections. A more detailed theoretical description of the formalism is presented in Refs. [42–44]. Following these works, the capture coefficient is computed as follows:

$$C = f \frac{2\pi}{\hbar} g V W_{if}^2 \sum_{m,n} w_m |\langle \chi_{im}|\Delta Q|\chi_{fn}\rangle|^2 \delta(E_{im} - E_{fn}), \tag{3}$$

where V is the supercell volume, g is the degeneracy factor of the final state of the defect, f is a scaling function that accounts for the Coulomb interaction between the carrier and the charged defect and the perturbation of the band edge wavefunction due to interaction with the charge defect energy level in the finite supercell.

Subscript indices i and f denote the initial and final charge states of the defect, ΔQ is the mass-weighted displacement between the equilibrium geometries of these states, E_{im} and E_{fn} denote the energies of the initial and final states, where m and n denote vibrational states, χ_{im} and χ_{fn} are their respective phonon wavefunctions, w_m is the thermal occupation number of the mth vibrational level of the initial electronic state. The temperature dependence of the capture coefficient is contained in the scaling function f and in the thermal occupation number w_m.

Finally, W_{if} represents the electron–phonon matrix element, which in the projected augmented wave method implemented in VASP is calculated as follows:

$$W_{if} = (\varepsilon_f - \varepsilon_i)\langle \psi_i|\hat{S}|\partial_Q \psi_f\rangle, \tag{4}$$

where ψ - the single-particle pseudo-wavefunction, ε - its corresponding eigenenergy, $\hat{S}$ - the overlap matrix due to the non-orthogonality of the pseudo-wavefunctions. W_{if} was computed by calculating the slope of $\langle \psi_i(0)|\hat{S}(0)|\psi_f(Q)\rangle$ as a function of Q. The calculations of matrix elements were performed using the NONRAD code [42,43].

Since the VBM in Si is triply degenerate, we calculated W_{if} as the root mean square of the matrix elements for each of the three bands for the hole capture process (see the discussion in Sec. F in [42]). For electron capture, W_{if} was calculated as the average of six conduction band valleys. It should be noted that the conduction band edge in this case does not correspond to the conduction band minimum (CBM) in Si. This is because the calculations were performed only with the Γ point, and due to band folding in supercells, the conduction band edge corresponds to the band edge at the X point. The latter is slightly higher in energy than the CBM, which is located along the $\Gamma \to$ X path (see Fig. S2 in the supplementary material). Therefore, we expect some overestimation of the calculated electron–phonon matrix elements (since $W_{if} \sim (\varepsilon_f - \varepsilon_i)^2$).

To calculate the phonon matrix elements $\langle \chi_{im}|\Delta Q|\chi_{fn}\rangle$, one-dimensional configuration coordinate diagrams (CCDs) were constructed. The diagram represents the potential energy surface (PES) of a defect in terms of the generalized coordinate Q. The construction was based on calculated energies for atomic structures corresponding to coordinates Q near the equilibrium configurations $Q_{0;i,f}$ of the initial and final states.

The CCDs were constructed in two steps. In the first step, the energies of ten structures corresponding to different Q coordinates near

$Q_{0;i,f}$ were computed. Quadratic interpolation was utilized to construct PES curves. In the second step, additional points were calculated corresponding to the estimated coordinate of the intersection of the curves, as well as points far beyond the considered intervals. Finally, PES was approximated by a fourth-order spline interpolation.

The second step is necessary to account for possible anharmonicity, which can cause PES curves to deviate from a quadratic shape. In practice, the second step can be omitted if the points calculated in the first step, as well as the intersection point, are well-described by a quadratic law. This often corresponds to the case where the ΔQ is small, and the intersection point lies near $Q_{0;i,f}$. More specifically, this corresponds to a small ionic relaxation during the charge state change.

The 1D Schrödinger equation was solved for each constructed PES, the solutions of which correspond to the phonon wavefunctions χ_{im} and χ_{fn}. The carrier capture cross-section was calculated as $\sigma = C/\langle v_{th}\rangle$, where $\langle v_{th}\rangle = \sqrt{3kT/m^*}$ is the carrier thermal velocity. The experimental values of the effective mass of an electron $m_e^* = 0.26m_0$ and the effective mass of a hole $m_e^* = 0.37m_0$, where m_0 represents the mass of an electron, were used [45]. The capture coefficient (Eq. (3)) and the 1D Schrödinger equation were calculated using tools implemented in the CarrierCapture.jl package [46].

It is important to note that the use of a one-dimensional model for CCDs can lead to an underestimation of the calculated cross-sections (see the discussion in Sec. V 5 in [42]). Therefore, the calculated cross-section values should be considered as a lower bound to the possible true value.

The defect transformation path was calculated using a climbing nudged elastic band (CL-NEB) method [47].

3. Results

3.1. Atomic structure

The relaxation results of V_3 are consistent with previous DFT studies [15–20]. The $V_{3,PHR}$ structure with C_{2v} symmetry (Fig. 1(a)) was obtained by removing three silicon atoms sequentially in the supercell, followed by relaxation. The $V_{3,FFC}$ structure with D_3 symmetry was obtained by removing three alternate silicon atoms in the hexagonal ring followed by relaxation.

The structure of $V_{3,PHR}$ is similar to the atomic configurations of E-centers and double vacancy by the presence of trimers formed by silicon atoms ($Si_1 - Si_2 - Si_3$ and $Si_1' - Si_2' - Si_3'$ in Fig. 1(a)) [22,41,48]. Analogously to E-centers and V_2, trimers in $V_{3,PHR}$ may have configurations shown in Fig. 1(b): breathing (B), resonant-bond (RB), pairing (P). The relaxation calculations showed that $V_{3,PHR}$ is in the P configuration for all charge states. The P configuration is more energetically favorable than the RB configuration by 0.20, 0.25, 0.20, 0.12, and 0.04 eV for charge states 2+, 1+, 0, 1−, and 2−, respectively. Except for the 2− state, the energy difference is an order of magnitude higher than $kT_{300\ K}$, which indicates a low probability of $V_{3,PHR}$ in the RB configuration.

For the 2− charge state, it can be assumed that the transformation $V_{3,PHR}^{2-}(P) \rightleftarrows V_{3,PHR}^{2-}(RB)$ is possible at room temperature. The question arises about the path of transformation. A possible path through the symmetric B configuration is unlikely due to its higher energy level compared to the P configuration by 0.45 eV. Therefore, the transformation path will include several intermediate configurations with lower symmetry.

To investigate the transformation path between P and RB configurations of $V_{3,PHR}^{2-}$, a CL-NEB calculation was performed, and the results are presented in Fig. 2. As expected, the minimum energy path (MEP) includes intermediate configurations of P and RB with lower symmetry. This path cannot occur at room temperature due to the high energy barrier. Therefore, we conclude that $V_{3,PHR}^{2-}$ exists only in the P configuration. This result is consistent with the findings in Ref. [19], in which the obtained electronic structure of $V_{3,PHR}$ corresponds to the P configuration (see Figs. 7 and 8 in Ref. [19] and the discussion below).
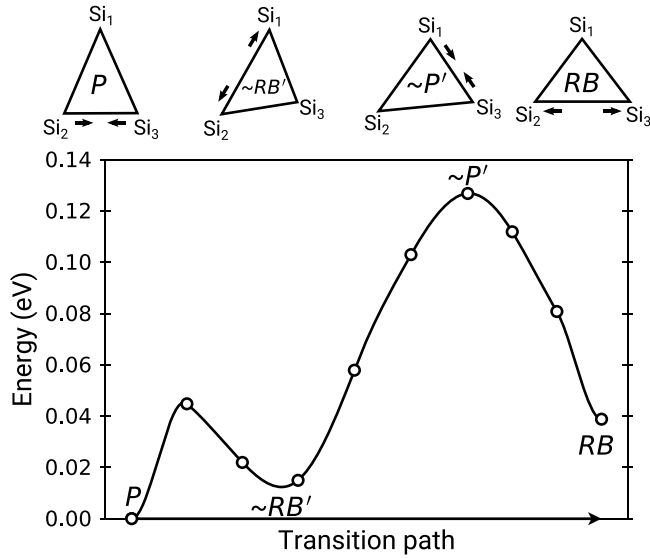
Fig. 2. Minimum energy path between $V_{3,PHR}^{2-}(P)$ and $V_{3,PHR}^{2-}(RB)$. The energy values are given relative to $V_{3,PHR}^{2-}(P)$. The prime symbol in the configuration notation (P' and RB') indicates a less symmetric structure due to the presence of the $Si_5' - Si_5$ dimer in Fig. 1(a).

Table 1
Calculated charge transition levels for V_3 in Si (This work), along with results from previous studies (Other works), and experimental data (DLTS).

Trans. level	$V_{3,PHR}$			$V_{3,FFC}$		
	This work	Other works	DLTS[c]	This work	Other work[c]	DLTS[c]
2+/1+	0.081	0.15[a] 0.13[b]	0.106	−0.174		
1+/0	0.206	0.29[a] 0.19[b]	0.193	−0.076		
0/1−	0.665	0.90[a] 0.68[b]	0.662	1.03	1.17	1.045
1−/2−	0.784	1.02[a] 0.75[b]	0.761	1.361		

[a] Ref. [19].
[b] Ref. [49].
[c] Ref. [19].

For the $V_{3,PHR}$, the Kohn–Sham levels are shown in Fig. 3(a). The electronic levels responsible for electronic activity of the defect (the low-energy b_1 and a_1 states) are clearly identified within the bandgap. The wavefunctions of these states are shown in Fig. 3(b). It is found that the defect function does not change its shape for the considered capture processes. In other words, the electron density localization region remains approximately constant. Therefore, the charge states 1+ and 1− were chosen to calculate W_{if}. A similar electronic structure was obtained in Ref. [19], except that the stable state was $S = 0$.
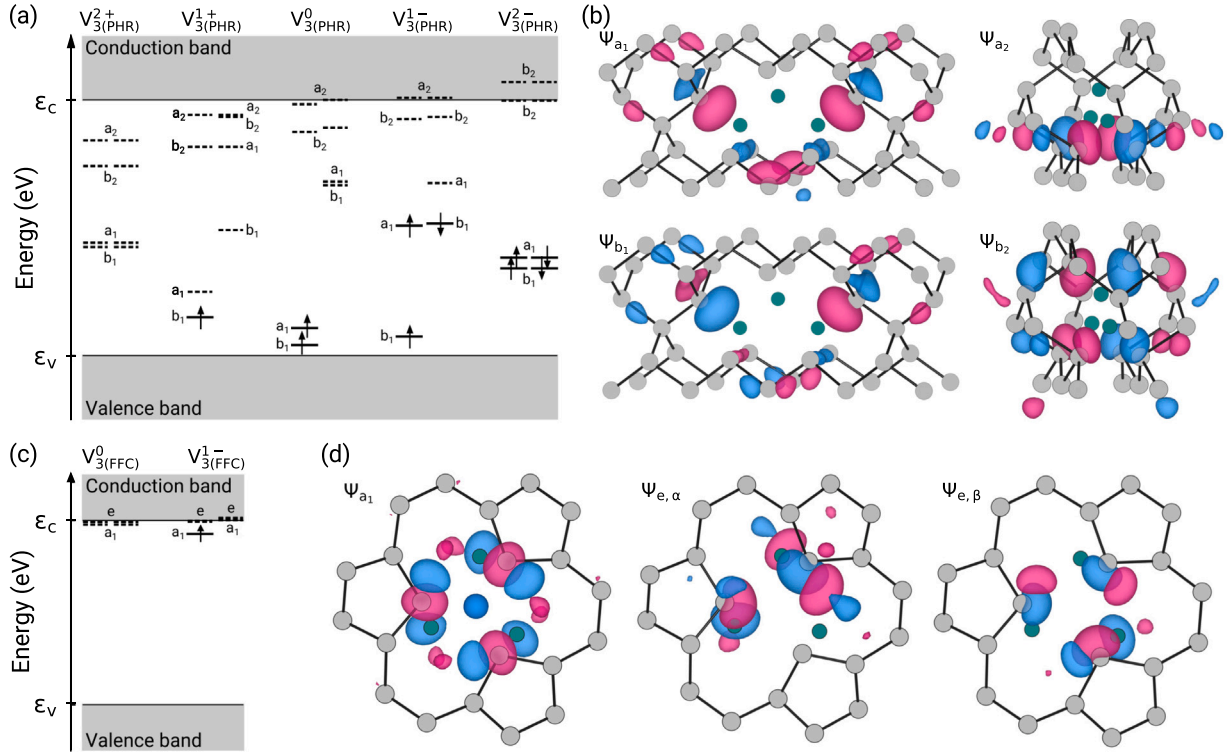
The electronic structure of $V_{3,FFC}$ is presented in Fig. 3(c). The unoccupied states a_1 and the doubly degenerate e are located near the conduction band edge. This is similar to the results in Ref. [19], but in our case, the states are closer to the conduction band edge. Upon capturing an electron, the filled spin-up state a_1 moves lower in energy. The wavefunctions corresponding to these states are shown in Fig. 3(d). As previously mentioned, in order to calculate matrix elements, the appropriate state in the bandgap should be clearly identified. For $V_{3,FFC}$, it is preferable to calculate the matrix elements in the 1− charge state.

3.3. Formation energy and transition levels

The calculated formation energy of $V_{3,PHR}$ and $V_{3,FFC}$ as a function of the Fermi level is presented in Figs. 4(a) and 4(b), respectively. It is found that $V_{3,PHR}$ has the four charge transition levels, while $V_{3,FFC}$ has one. The calculated values of the thermodynamic charge transition levels, compared with experimental data and previous works, are provided in Table 1. They are in agreement with experimental DLTS data. The Calculation results in Ref. [49] using GGA and extrapolation to infinite supercell size are also close to experimental data, in contrast to Ref. [19], in which an LDA functional and marker method were employed. It is critical to obtain reliable values for charge transition levels to calculate capture cross-sections. Thus, we conclude that using the semi-empirical marker method is not recommended, and relying on a complete *ab initio* approach is preferable.

Comparison of the formation energies of $V_{3,PHR}$ and $V_{3,FFC}$ is presented in Fig. 4(c). As expected, in agreement with experimental data and the results of previous studies, the FFC configuration is energetically favorable in the neutral charge state. In the case of the charged defect, the PHR configuration with a charge of 2− is the favorable state. The transition from the stable neutral to the stable charged state $V_{3,FFC}^0/V_{3,PHR}^{2-}$ corresponds to a Fermi level of 0.90 eV. In Ref. [19], the value of this transition corresponds to an energy of 1.06 eV, which is significantly higher than our value. We also did not find the transition $V_{3,FFC}^0/V_{3,PHR}^{2-}$', which in Ref. [19] corresponds to a Fermi level of 0.11 eV. The reason for such discrepancy, as mentioned earlier, could be the marker method used in Ref. [19] to estimate transition levels.

Thus, we have found that the trivacancy exists in the neutral FFC configuration within the Fermi level range of 0 to 0.90 eV. Above these values the trivacancy is in the $V_{3,PHR}^{2-}$ configuration.

3.2. Electronic structure

The spin-polarized calculations of the relaxed structures indicate that the electronic state of $V_{3,PHR}^0$ with spin $S = 1$ is 2 meV more stable than the spin $S = 0$ state. Previous works have not agreed on an energetically favorable spin state. Refs. [18,49] report the energetically favorable state with spin $S = 1$, while Ref. [19] reports the spin $S = 0$ state. Although the energy difference between the states is small and does not affect the formation energy and transition levels, the choice of state for cross-section calculations is significant because specifying a single-electron level involved in the capture process is necessary to calculate matrix elements. For further calculations, the $S = 1$ state will be utilized.

For the other charge states of $V_{3,PHR}$ and $V_{3,FFC}$, spin states with the minimum possible spin were found to be favorable. This means $S = 0$ for even charge states and $S = 1/2$ for odd charge states.

To calculate W_{if}, one needs to select the charge state of the defect in which the calculation is to be performed. The main selection criterion is that the defect states in which the carriers are captured must be clearly identified in the bandgap [42,43]. It is also useful to verify that the defect wavefunction does not change significantly during the capture process. This indicates that the calculated capture cross-sections in each of the two charge states will be negligibly different (see the discussion in Sec. III F in [42]).

In most cases, it is most convenient to calculate W_{if} with a neutral charge state to avoid the difficulties that arise when using a charged supercell. However, there may be situations where using a charged state is necessary or more practical. In our case, it is computationally advantageous to calculate W_{if} in the charge states 1+ and 1−. Indeed, a series of matrix element calculations for these states will allow us to directly calculate the capture cross-sections for the transitions from $\varepsilon(2+/1+)$ to $\varepsilon(1-/2-)$.

The appropriate charge states for the calculation of W_{if} were determined by analyzing the electronic band structure of the defect.

The atomic structure of $V_{3,FFC}$ obtained from the relaxation coincides with the one obtained in Ref. [19]. By examining the local atomic environment of $V_{3,FFC}$, we found comparable bond lengths and angles (see the discussion in Sec. V A in Ref. [19]).

Fig. 3. Single-electron states of (a) $V_{3,PHR}$ and (c) $V_{3,FFC}$. Solid lines represent occupied states, while dashed lines represent empty states. Spin-up and spin-down states are indicated by vertical arrows. The isosurfaces of the calculated single-electron wavefunctions for the Kohn–Sham states are illustrated in (b) and (d) for $V_{3,PHR}$ and $V_{3,FFC}$, respectively (0.0006 $e/\text{Å}$). The positive phase of the wavefunction is represented in pink, and the negative phase in blue.

Table 2
Calculated energy barrier E_b, electron–phonon coupling W_{if}, calculated carrier capture cross-sections at room temperature $\sigma^{T=300\ \text{K}}$, and experimental apparent cross-section σ_{exp} for $V_{3,PHR}$ and $V_{3,FFC}$.

Defect	$V_{3,PHR}$						$V_{3,FFC}$	
Transition	2+/1+	1+/0	0/1−		1−/2−		0/1−	
Carrier	h+	h+	h+	e−	h+	e−	h+	e−
E_b (eV)	0.005	0.180	0.155	0.086	0.713	0.003	4.895	0.086
W_{if} ($\frac{\text{meV}}{\text{amu}^{1/2}\text{Å}}$)	34	14.7	0.5	14.8	0.4	31	1.8	31
$\sigma^{T=300\ \text{K}}$ (cm^2)	6.12×10^{-15}	2.34×10^{-16}	5.58×10^{-19}	3.79×10^{-16}	3.83×10^{-23}	9.73×10^{-17}	1.82×10^{-37}	2.24×10^{-17}
σ_{exp} (cm^2)[a]	6.18×10^{-15}	3.09×10^{-15}	–	2.4×10^{-15}	–	2.15×10^{-15}	–	3.7×10^{-15}

[a] Values for holes are taken from Ref. [17], for electrons from Ref. [18].

3.4. Capture cross-section

The calculated values of barriers for the non-radiative process E_b (calculated from the diagrams), electron–phonon matrix element values W_{if}, calculated cross-section values at T = 300 K, as well as experimental apparent capture cross-sections[1] [17,18] are presented in Table 2.

---

[1] The carrier emission rate is determined as $e_{e,h} = \sigma_{e,h} v_{e,h} N_{c,v} \exp(-\Delta E/kT)$, where ΔE is the difference between the defect level and the valence band edge in the case of hole emission, and the difference between the conduction band edge and the defect level in the case of electron emission. Traditionally, the dependence of $e_{e,h}$ on T is measured using DLTS technique. The Arrhenius plot $\ln(e_{e,h}/T^2)$ versus $1/kT$ (where T^2 accounts for the temperature dependence of thermal velocity $v_{e,h}$ and effective density of states $N_{c,v}$) allows the determination of ΔE as the slope. The vertical intercept determines the $\sigma_{e,h}(T = \infty)$, the so-called apparent capture cross-section. This method assumes a temperature-independent capture cross-section, which may not be true in reality, affecting the accuracy of ΔE determination.

3.4.1. Capture cross-section of $V_{3,FFC}$

First, let us examine the $\varepsilon(0/1−)$ transition for the $V_{3,FFC}$ configuration. The calculated CCD is presented in Fig. 5(a). In contrast to electron capture, the barrier for hole capture is above the values at which a non-radiative process can occur (Table 2). The complete diagram, including all additional Q coordinates from the second construction step (see section 2), is presented in the supplementary material in Fig. S3. When calculating the capture cross-sections, the process with a large barrier can be neglected. However, in Ref. [20], possible mechanisms of the $V_{3,FFC} \rightarrow V_{3,PHR}$ transformation were considered, and the most probable of them is the one in which the capture of electron and hole by $V_{3,FFC}$ occurs sequentially (see mechanism 6 in Ref. [19]). Thus, the cross-section for hole capture was calculated to estimate the possibility of this mechanism.

The calculated dependencies of electron and hole capture cross-sections on temperature are shown in Fig. 5(b). As expected, due to the large barrier value, the hole capture cross-section is negligibly small, excluding the proposed transformation mechanism. The calculated electron capture cross-section is lower than the experimental value. A
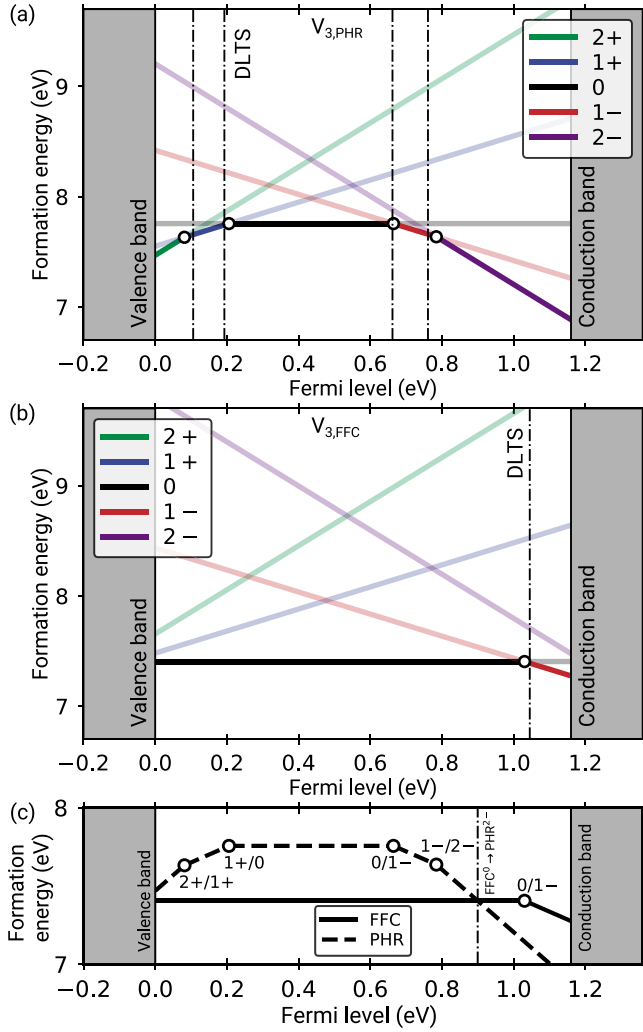
Fig. 4. The calculated formation energy as a function of Fermi level for (a) $V_{3,PHR}$, (b) $V_{3,FFC}$. (c) Comparison of the formation energies of energetically favorable charge states between $V_{3,PHR}$ and $V_{3,FFC}$. The circles indicate the intersection points of the formation energy dependencies corresponding to the charge transition levels. On (a) and (b), experimental DLTS values are represented by vertical lines. On (c), the vertical line indicates the level of the transition $V_{3,FFC}^0/V_{3,PHR}^{2-}$.

discussion of the discrepancy with experimental data is presented in the next section.

3.4.2. Capture cross-section of $V_{3,PHR}$

Although the $V_{3,PHR}$ configuration is energetically favorable only at the Fermi level above 0.9 eV, it also requires careful analysis of capture cross-sections. Immediately after irradiation, the trivacancy is in the $V_{3,PHR}$ configuration, which at room temperature exists for several weeks before transforming into $V_{3,FFC}$ [15–20].

The calculated diagrams for $V_{3,PHR}$ are presented in Fig. 6. The complete diagrams with all Q coordinates for donor levels $\varepsilon(2+/1+)$ and $\varepsilon(1+/0)$ are presented in the supplementary material in Fig. S3. For donor levels there is no intersection of the potential energy curves for the electron capture process. Non-radiative electron capture is therefore unlikely. The reason for this may be the use of the 1D approximation. Alternatively, carrier capture may occur through another mechanism, such as quantum tunneling. In any case, the cross-sections for such a process will be negligibly small and will not be considered further. Special attention should be paid to the $\varepsilon(0/1-)$ transition when considering acceptor levels. This is because the level is located near the middle of the bandgap ($\varepsilon(0/1-) = 0.665$ eV) and has low barrier values (Table 2),
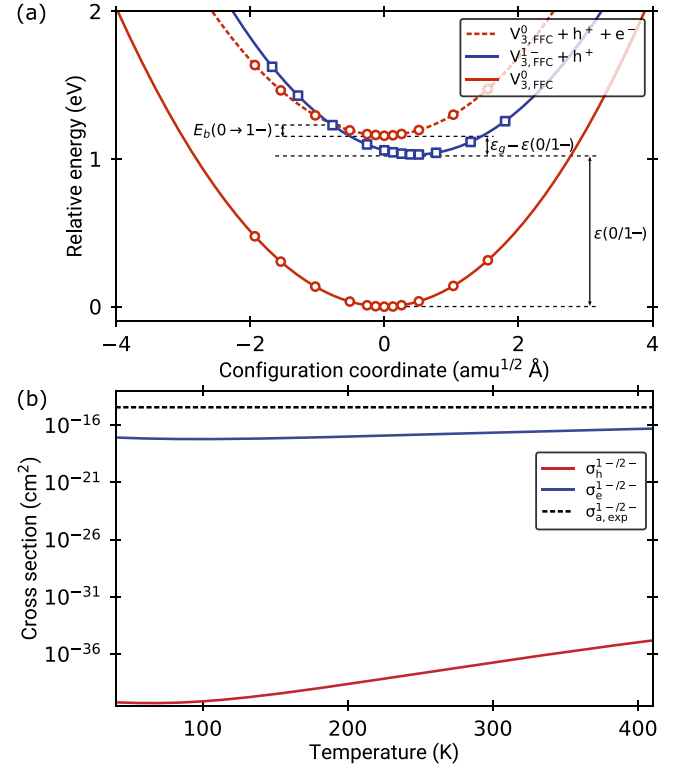

Fig. 5. Calculated (a) CCD, (b) hole (red solid line) and electron (blue solid line) capture cross-section as a function of temperature for the $\varepsilon(0/1-)$ transition level of $V_{3,FFC}$. In (a), the energy values calculated by DFT are indicated by the points, while the line represents the fourth-order spline interpolation fit. In (b), the dashed blue line shows the experimental apparent cross-section.

which suggest that it can act as a recombination center. The second acceptor level $\varepsilon(1-/2-)$ is located closer to the conduction band and has a larger barrier to the hole capture process.

First, let us examine the donor levels. The calculated hole capture cross-sections as a function of temperature along with the experimental apparent values are presented in Fig. 7(a)–7(b). The temperature dependence of the hole capture cross-sections is significant. At about room temperature, the calculated values are close to the experimental ones (Table 2), while at high temperatures they are larger. As mentioned earlier, the one-dimensional approximation tends to underestimate capture cross-sections (Section 2). It is reasonable to assume that the truly hole capture cross-section is temperature dependent, since the calculated values are higher than the experimental apparent values at high temperatures. Additionally, this assumption is supported by the fact that peaks of DLTS signals for donor levels were observed at $T \approx 50$ K (for $\varepsilon(2+/1+)$) and $T \approx 120$ K (for $\varepsilon(1+/0)$) [17].

For the acceptor levels, the calculated capture cross-sections as a function of temperature are presented in Fig. 2(c)-2(d). For the $\varepsilon(0/1-)$ acceptor level, the results indicate that it can act as a recombination center at room temperature, since it has the appropriate cross-section values (Table 2). The $\varepsilon(1-/2-)$ level has a smaller hole capture cross-section and is located further from the middle of the bandgap. Therefore, it is unlikely to act as an effective recombination center.

The calculated electron capture cross-sections for the acceptor levels, as in the case of $V_{3,FFC}$, are about two orders of magnitude smaller than the experimental apparent ones. For the $\varepsilon(1-/2-)$ level, the calculated electron capture cross-section shows a weak temperature dependence, and if this is indeed the case, it should agree with the apparent experimental one. However, in this case, an underestimation of two orders of magnitude may suggest a systematic error.
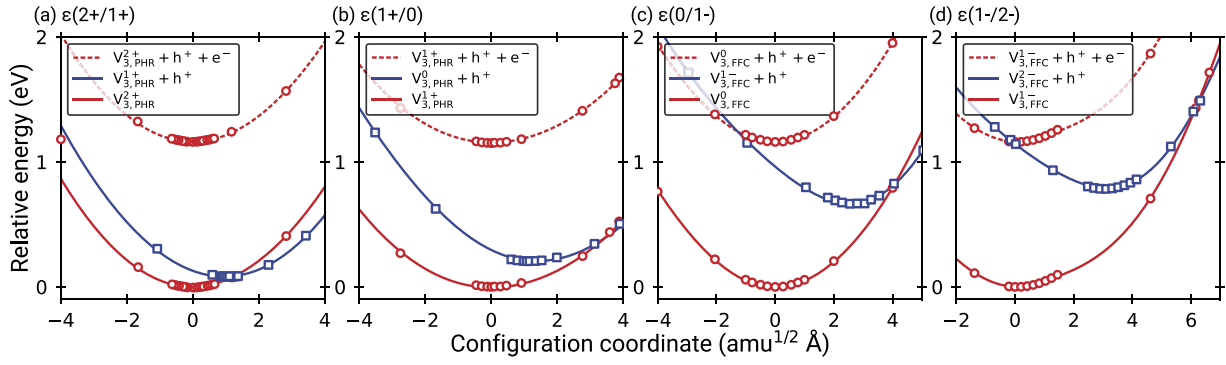
Fig. 6. Calculated CCDs for $V_{3,PHR}$. The energy values calculated by DFT are indicated by the points, while the line represents the fourth-order spline interpolation fit.
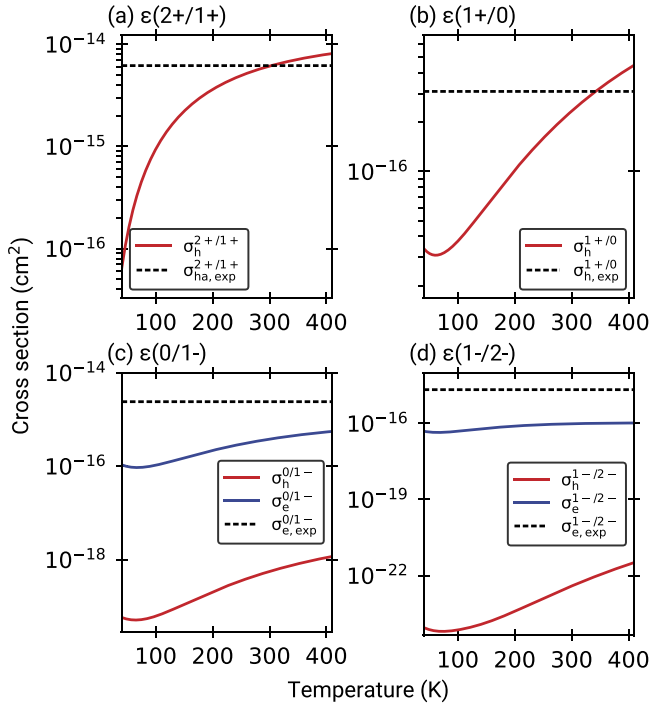

Fig. 7. Calculated capture cross-sections for holes (red solid line) and electrons (blue solid line) as a function of temperature for $V_{3,PHR}$. Black dashed lines represent experimental apparent cross-sections values.

3.4.3. Analysis of possible error sources

Thus, the electron capture cross-sections have a systematic error. In addition to the one-dimensional formalism used to calculate the capture cross-section, there are several other potential sources of error that may affect the accuracy of the calculations. As noted in Section 2, using the Γ point in calculations that do not correspond to the CBM in Si may lead to an error. However, in this case, it is expected to overestimate the cross-section values. Another possible reason for the discrepancy between calculations and DLTS experiments is the difference in temperature. Calculations use values for zero temperature, while DLTS experiments are conducted at finite temperatures, where the bandgap width will be smaller.

The influence of these two factors on the electron capture cross-section can be estimated approximately. Consider the $\varepsilon(0/1-)$ level for $V_{3,PHR}$ as an example. The calculated gap at the Γ point is $\varepsilon_{g,\Gamma} = 1.20$ eV. If we were considering a true conduction band minimum, then the conduction band edge would decrease by $\Delta\varepsilon = 0.04$ eV in accordance with the calculated band gap $\varepsilon_g = 1.16$ eV. It is assumed that the energy level of the defect does not depend on the wave vector. In this case, the ratio of the electron capture cross-section calculated at the Γ point (σ_e) to the cross-section calculated at the k point corresponding to the conduction band minimum ($\sigma_{e,CBM}$) is $\sigma_e/\sigma_{e,CBM} \sim (\varepsilon_f - \varepsilon_i)^2/(\varepsilon_f - \varepsilon_i - \Delta\varepsilon)^2 \approx 1.15$. The values $\varepsilon_{i,f}$ are taken from the calculations for $V_{3,PHR}^{1-}$. As a result, the error caused by this factor is negligible compared to two orders of magnitude.

Considering that the bandgap at room temperature is $\varepsilon_{g,300\,K} = 1.12$ eV [32], we can estimate the influence of the second factor. Also, it is assumed that the position of the charge transition level remains constant. This will cause the upper curve on the CCD (Fig. 7(c)) to move down by the value of $\varepsilon_g - \varepsilon_{g,300\,K} = 0.04$ eV, resulting in a decrease in the barrier value. The recalculated barrier value is $E_{b,300\,K} = 0.047$ eV. As the carrier capture process is temperature-activated, the capture rate at high temperatures can be approximated by a function of the form [42]

$$C = C_0 + C_1\exp(-E_b/kT). \tag{5}$$

Assuming that $C_0 \ll C_1$, the calculated cross-section (σ_e) to the cross-section corresponding to the room temperature bandgap ($\sigma_{e,300\,K}$) can be estimated as $\frac{\sigma_e}{\sigma_{e,300\,K}} \sim \frac{\exp(-E_b/kT_{300\,K})}{\exp(-E_{b,300\,K}/kT_{300\,K})} \approx 0.24$. Thus, at room temperature, the calculated electron capture cross-section is underestimated by a factor of four due to the change in the bandgap. However, it is still significantly less than two orders of magnitude. Although the estimates performed are approximate, we assume that the main source of underestimation is the one-dimensional approximation. The assumption is also supported by the results presented in Ref. [50], where different formalisms for calculating capture cross-sections have been compared, and it is shown that the one-dimensional approximation also underestimates the capture cross-section.

Therefore, the calculated cross-sections for electron and hole capture should be interpreted as a lower bound. These values can be used to estimate the current generated in the pn-junction diodes caused by radiation-induced trivacancy formation.

### 3.5. Generation current density estimation

This section examines the effect of the two V_3 configurations (PHR and FFC) on the generation current. Neglecting the Poole-Frenkel effect [51], the generation current density in a reverse-biased diode caused by defect level is defined by the Shockley–Read–Hall model as [52,53]

$$J_{gen} = e \int_0^W \left[\sum_i \eta_i N_i\right] dx \tag{6}$$

where η_i is the recombination efficiency of a defect i, while N_i represents defect concentration within the width of the space-charge region W. The recombination efficiency is defined by

$$\eta = \frac{\sigma_e v_e N_c \sigma_h v_h N_v \exp(-\frac{\varepsilon_g}{kT})}{\sigma_e v_e N_c \exp(-\frac{\varepsilon_c - \varepsilon_t}{kT}) + \sigma_h v_h N_v \exp(-\frac{\varepsilon_t - \varepsilon_v}{kT})} \tag{7}$$
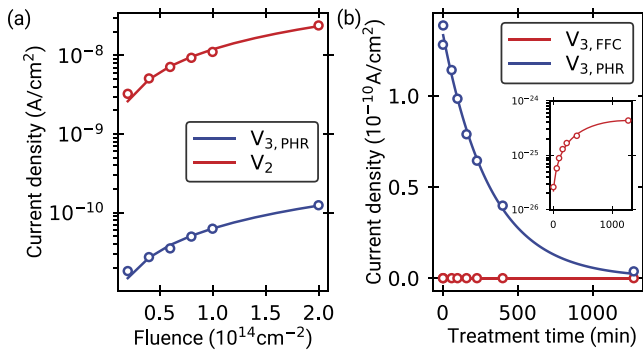
Fig. 8. (a) calculated generation current caused by V_2 and $V_{3,PHR}$ as a function of 4 MeV electrons fluence in an epi-Si p$^+$-n-p$^+$ diode, (b) changes in the generation current of the $V_{3,PHR}$ and $V_{3,FFC}$ configurations in reverse-biased epi-Si p$^+$-n diode upon isothermal annealing at $T = 330$ K with applied reverse bias of -12 V. In (a) the experimental data of concentration V_2 and $V_{3,PHR}$ are taken from Ref. [20]. In (b) the experimental data of concentration $V_{3,PHR}$ and $V_{3,FFC}$ are taken from Ref. [19].

where $N_{c,v}$ is the effective density of states in the conduction and valence bands, respectively. Eqs. (6)–(7) model a defect with a single electron level. In practice, we are interested in levels with high recombination efficiency, which typically correspond to positions near the middle of the bandgap. Therefore, it is often possible to ignore all levels of defects except the level with the highest recombination efficiency and use a single level model.

The electron capture coefficient for the $V_{3,PHR}$ donor levels is assumed to be negligibly small, resulting in zero recombination efficiency. For acceptor levels, the recombination efficiency at $T = 300$ K is $\eta = 1.3 \times 10^{-3}$ s^{-1} for the $\varepsilon(0/1-)$ level and $\eta = 0.9 \times 10^{-9}$ s^{-1} for $\varepsilon(1-/2-)$. Therefore, the $\varepsilon(1-/2-)$ level can be neglected. Considering only the $\varepsilon(0/1-)$ level is consistent with experimental observations, where this level has been shown to be one of the main sources of generation current in silicon diodes [54].

To estimate the generation current, we used experimental data on the concentration of the double vacancy (V_2) and $V_{3,PHR}$ as a function of the fluence of 4 MeV electrons in an epi-Si p$^+$-n-p$^+$ diode (Fig. 3 in Ref. [20]). The values of the charge transition levels and the capture cross-sections for V_2 were taken from the experimental data [55,56]. Assuming that defects in the space charge region are uniformly distributed, we set $W = 1$ cm in the Eq. (6) to examine the relationship between the generation currents from each defect. Fig. 8(a) shows the dependence of J_{gen} on electron fluence for V_2 and $V_{3,PHR}$. The contribution to the total generation current from V_2 is about two orders of magnitude larger than the contribution from $V_{3,PHR}$. But, if we assume that the calculated capture cross-sections of $V_{3,PHR}$ are underestimated, the true contribution of $V_{3,PHR}$ may be larger and comparable to V_2. Therefore, it is important to consider $V_{3,PHR}$ as a potential source of generation current when modeling radiation damage in silicon.

For $V_{3,FFC}$, the calculated recombination efficiency is negligibly small, $\eta = 3 \times 10^{-28}$ s^{-1}. The result confirms the conclusions that $V_{3,FFC}$ is an electrically neutral defect. Fig. 8(b) shows the relationship between the generation current and the annealing time for both defect configurations during the $V_{3,PHR} \rightarrow V_{3,FFC}$ transformation (experimental data were taken from Ref. [18]). The transformation results in the removal of the generation current from V_3. Therefore, the calculations confirm that the annealing-induced transformation indeed leads to the recovery of damaged silicon devices.

4. Conclusions

In this study, using first-principles methods, we presented an investigation of the bistable trivacancy complex in silicon. We obtained atomic structures for V_3 (PHR and FFC) that confirm previous experimental

and theoretical findings. Additional studies on possible symmetry configurations showed that $V_{3,PHR}$ corresponds to a pairing geometry in all charge states. Thermodynamic charge transition levels calculated using the HSE06 functional are in excellent agreement with experimental data. The formation energy calculations also confirmed previous findings that over almost the entire bandgap, the stable configuration of the trivacancy is the $V_{3,FFC}$ structure in the neutral charge state. The transition from $V_{3,FFC}$ to $V_{3,PHR}$ was observed at the Fermi level of 0.9 eV, with $V_{3,PHR}$ corresponding to the 2− charge state.

The calculated hole capture cross-sections are in good agreement with experimental values for donor levels of $V_{3,PHR}$. On the other hand, the calculated electron capture cross-sections for acceptor levels of $V_{3,PHR}$ and $V_{3,FFC}$ are systematically about two orders of magnitude smaller than experimental values. A main source of error, we assume, is the use of only a one-dimensional model in the calculations. However, it is expected to suffer from such an error when calculating the cross-section using a one-dimensional model, and the calculated values should be interpreted as a lower bound.

Using the calculated capture cross-section values, we also computed the generation current for each defect level at $T = 300$ K. The results show that the acceptor level $\varepsilon(0/1-)$ is the effective recombination generation center for V_3. This level may be one of the sources of current generation in silicon diode devices under irradiation. Calculations show also that the annealing-induced transformation $V_{3,PHR} \rightarrow V_{3,FFC}$ can lead to the recovery of silicon diodes.

CRediT authorship contribution statement

Vladislav Pelenitsyn: Writing – original draft, Visualization, Methodology, Investigation. **Pavel Korotaev:** Writing – review & editing, Supervision.

Declaration of competing interest

The authors declare that they have no known competing financial interests or personal relationships that could have appeared to influence the work reported in this paper.

Data availability

Data will be made available on request.

Appendix A. Supplementary data

Supplementary material related to this article can be found online at https://doi.org/10.1016/j.commatsci.2024.113226.

References

[1] C. Claeys, E. Simoen, Basic Radiation Damage Mechanisms in Semiconductor Materials and Devices, Springer Berlin Heidelberg, Berlin, Heidelberg, 2002, pp. 9–52, URL http://dx.doi.org/10.1007/978-3-662-04974-7_2.

[2] B.N. Mukashev, K.A. Abdullin, Y.V. Gorelkinskii, Metastable and bistable defects in silicon, Phys.-Usp. 43 (2) (2000) 139, URL http://dx.doi.org/10.1070/PU2000v043n02ABEH000649.

[3] V.P. Markevich, M. Vaqueiro-Contreras, S.B. Lastovskii, L.I. Murin, M.P. Halsall, A.R. Peaker, Electron emission and capture by oxygen-related bistable thermal double donors in silicon studied with junction capacitance techniques, J. Appl. Phys. 124 (22) (2018) 225703, arXiv:https://doi.org/10.1063/1.5053805 URL http://dx.doi.org/10.1063/1.5053805.

[4] G. Watkins, 35 Years of defects in semiconductors: What next? in: Defects in Semiconductors 17 143 of Materials Science Forum, Trans Tech Publications Ltd, 1993, pp. 9–20, http://dx.doi.org/10.4028/www.scientific.net/MSF.143-147.9.

[5] G. Watkins, Defect metastability and bistability, in: Defects in Semiconductors 15 38of Materials Science Forum, Trans Tech Publications Ltd, 1989, pp. 39–50, http://dx.doi.org/10.4028/www.scientific.net/MSF.38-41.39.

[6] A. Chantre, Introduction to defect bistability, Appl. Phys. A 48 (1) (1989) 3–9, URL http://dx.doi.org/10.1007/BF00617758.

[7] G. Baraff, Introduction to metastability: Configuration coordinate diagrams, in: Defects in Semiconductors 14 10of Materials Science Forum, Trans Tech Publications Ltd, 1986, pp. 377–386, http://dx.doi.org/10.4028/www.scientific.net/MSF.10-12.377.

[8] M. Nisenoff, H.Y. Fan, Electron spin resonance in neutron-irradiated silicon, Phys. Rev. 128 (1962) 1605–1613, http://dx.doi.org/10.1103/PhysRev.128.1605, URL https://link.aps.org/doi/10.1103/PhysRev.128.1605.

[9] W. Jung, G.S. Newell, Spin-1 centers in neutron-irradiated silicon, Phys. Rev. 132 (1963) 648–662, http://dx.doi.org/10.1103/PhysRev.132.648, URL https://link.aps.org/doi/10.1103/PhysRev.132.648.

[10] K.L. Brower, Structure of multiple-vacancy (oxygen) centers in irradiated silicon, Radiat. Eff. 8 (3–4) (1971) 213–219, arXiv:https://doi.org/10.1080/00337577108231031 URL http://dx.doi.org/10.1080/00337577108231031.

[11] Y.H. Lee, Y.M. Kim, J.W. Corbett, New epr spectra in neutron-irradiated silicon, Radiat. Eff. 15 (1–2) (1972) 77–84, arXiv:https://doi.org/10.1080/00337577208232584 URL http://dx.doi.org/10.1080/00337577208232584.

[12] Y.-H. Lee, J.W. Corbett, Epr study of defects in neutron-irradiated silicon: Quenched-in alignment under ⟨110⟩-uniaxial stress, Phys. Rev. B 9 (1974) 4351–4361, http://dx.doi.org/10.1103/PhysRevB.9.4351, URL https://link.aps.org/doi/10.1103/PhysRevB.9.4351.

[13] D.V. Makhov, L.J. Lewis, Stable fourfold configurations for small vacancy clusters in silicon from ab initio calculations, Phys. Rev. Lett. 92 (2004) 255504, http://dx.doi.org/10.1103/PhysRevLett.92.255504, URL https://link.aps.org/doi/10.1103/PhysRevLett.92.255504.

[14] J.L. Hastings, S.K. Estreicher, P.A. Fedders, Vacancy aggregates in silicon, Phys. Rev. B 56 (1997) 10215–10220, http://dx.doi.org/10.1103/PhysRevB.56.10215, URL https://link.aps.org/doi/10.1103/PhysRevB.56.10215.

[15] V. Markevich, A. Peaker, S. Lastovskii, L. Murin, J. Coutinho, A. Markevich, V. Torres, P. Briddon, L. Dobaczewski, E. Monakhov, B. Svensson, Trivacancy in silicon: A combined dlts and ab-initio modeling study, Physica B 404 (23) (2009) 4565–4567, http://dx.doi.org/10.1016/j.physb.2009.08.142, URL https://www.sciencedirect.com/science/article/pii/S0921452609008709.

[16] V. Markevich, A. Peaker, B. Hamilton, S. Lastovskii, L. Murin, J. Coutinho, A. Markevich, M. Rayson, P. Briddon, B. Svensson, Reconfigurations and diffusion of trivacancy in silicon, Physica B 407 (15) (2012) 2974–2977, http://dx.doi.org/10.1016/j.physb.2011.08.001, URL https://www.sciencedirect.com/science/article/pii/S0921452611007393. 26th International Conference on Defects in Semiconductors.

[17] V.P. Markevich, A.R. Peaker, B. Hamilton, S.B. Lastovskii, L.I. Murin, J. Coutinho, V.J.B. Torres, L. Dobaczewski, B.G. Svensson, Structure and electronic properties of trivacancy and trivacancy-oxygen complexes in silicon, Phys. Status Solidi (a) 208 (3) (2011) 568–571, https://doi.org/10.1002/pssa.201000265. arXiv:https://onlinelibrary.wiley.com/doi/pdf/10.1002/pssa.201000265 URL https://onlinelibrary.wiley.com/doi/abs/10.1002/pssa.201000265.

[18] V.P. Markevich, A.R. Peaker, S.B. Lastovskii, L.I. Murin, J. Coutinho, V.J.B. Torres, P.R. Briddon, L. Dobaczewski, E.V. Monakhov, B.G. Svensson, Trivacancy and trivacancy-oxygen complexes in silicon: Experiments and ab initio modeling, Phys. Rev. B 80 (2009) 235207, http://dx.doi.org/10.1103/PhysRevB.80.235207, URL https://link.aps.org/doi/10.1103/PhysRevB.80.235207.

[19] J. Coutinho, V.P. Markevich, A.R. Peaker, B. Hamilton, S.B. Lastovskii, L.I. Murin, B.J. Svensson, M.J. Rayson, P.R. Briddon, Electronic and dynamical properties of the silicon trivacancy, Phys. Rev. B 86 (2012) 174101, http://dx.doi.org/10.1103/PhysRevB.86.174101, URL https://link.aps.org/doi/10.1103/PhysRevB.86.174101.

[20] V.P. Markevich, A.R. Peaker, B. Hamilton, S. Lastovskii, L.I. Murin, J. Coutinho, M.J. Rayson, P.R. Briddon, B.G. Svensson, The trivacancy and trivacancy-oxygen family of defects in silicon, in: Gettering and Defect Engineering in Semiconductor Technology XV, 205 of Solid State Phenomena, Trans Tech Publications Ltd, 2014, pp. 181–190, http://dx.doi.org/10.4028/www.scientific.net/SSP.205-206.181.

[21] J.G.M. Shaw, P. Briddon, Marker-Method Calculations for Electrical Levels using Gaussian-Orbital Basis Sets, Springer Berlin Heidelberg, Berlin, Heidelberg, 2007, pp. 69–94, URL http://dx.doi.org/10.1007/11690320_4.

[22] G. Herrero Saboya, Defects in Silicon : Revisiting Theoretical Frameworks To Guide Ab Initio Characterization Theses, Université Paul Sabatier - Toulouse III, 2020, URL https://theses.hal.science/tel-03215768.

[23] C. Freysoldt, B. Grabowski, T. Hickel, J. Neugebauer, G. Kresse, A. Janotti, C.G. Van de Walle, First-principles calculations for point defects in solids, Rev. Modern Phys. 86 (1) (2014) 253–305, http://dx.doi.org/10.1103/RevModPhys.86.253, URL https://link.aps.org/doi/10.1103/RevModPhys.86.253.

[24] L.J. Sham, M. Schluter, Density-functional theory of the band gap, Phys. Rev. B 32 (1985) 3883–3889, http://dx.doi.org/10.1103/PhysRevB.32.3883, URL https://link.aps.org/doi/10.1103/PhysRevB.32.3883.

[25] D. Bagayoko, Understanding density functional theory (dft) and completing it in practice, AIP Adv. 4 (12) (2014) 127104, arXiv:https://doi.org/10.1063/1.4903408 URL http://dx.doi.org/10.1063/1.4903408.

[26] G. Kresse, J. Furthmüller, Efficient iterative schemes for ab initio total-energy calculations using a plane-wave basis set, Phys. Rev. B 54 (16) (1996) 11169–11186, http://dx.doi.org/10.1103/PhysRevB.54.11169, URL https://link.aps.org/doi/10.1103/PhysRevB.54.11169.

[27] G. Kresse, D. Joubert, From ultrasoft pseudopotentials to the projector augmented-wave method, Phys. Rev. B 59 (1999) 1758, http://dx.doi.org/10.1103/PhysRevB.59.1758, URL https://journals.aps.org/prb/abstract/10.1103/PhysRevB.59.1758.

[28] J. Heyd, G.E. Scuseria, M. Ernzerhof, Hybrid functionals based on a screened Coulomb potential, J. Chem. Phys. 118 (18) (2003) 8207–8215, http://dx.doi.org/10.1063/1.1564060, URL https://aip.scitation.org/doi/10.1063/1.1564060.

[29] J. Heyd, G.E. Scuseria, Efficient hybrid density functional calculations in solids: Assessment of the Heyd–Scuseria–Ernzerhof screened Coulomb hybrid functional, J. Chem. Phys. 121 (3) (2004) 1187–1192, http://dx.doi.org/10.1063/1.1760074, URL https://aip.scitation.org/doi/10.1063/1.1760074.

[30] J. Heyd, G.E. Scuseria, M. Ernzerhof, Erratum: Hybrid functionals based on a screened Coulomb potential, J. Chem. Phys. 124 (21) (2006) 219906, http://dx.doi.org/10.1063/1.2204597, URL https://aip.scitation.org/doi/10.1063/1.2204597.

[31] Y. Okada, Y. Tokumaru, Precise determination of lattice parameter and thermal expansion coefficient of silicon between 300 and 1500 k, J. Appl. Phys. 56 (2) (1984) 314–320, URL http://dx.doi.org/10.1063/1.333965.

[32] O. Madelung, U. Rössler, M.E. Schulz, Silicon (Si), Band Structure: Datasheet from Landolt-Börnstein - Group Iii Condensed Matter · Volume 41a1β: Group Iv Elements, Iv-Iv and Iii-V Compounds. Part B - Electronic, Transport, Optical and Other Properties in Springermaterials, 2002, http://dx.doi.org/10.1007/10832182_432, URL https://materials.springer.com/lb/docs/sm_lbs_978-3-540-31356-4_432.

[33] J.P. Perdew, K. Burke, M. Ernzerhof, Generalized gradient approximation made simple, Phys. Rev. Lett. 77 (18) (1996) 3865–3868, http://dx.doi.org/10.1103/PhysRevLett.77.3865, URL https://link.aps.org/doi/10.1103/PhysRevLett.77.3865.

[34] S.B. Zhang, J.E. Northrup, Chemical potential dependence of defect formation energies in gaas: Application to ga self-diffusion, Phys. Rev. Lett. 67 (1991) 2339–2342, http://dx.doi.org/10.1103/PhysRevLett.67.2339, URL https://link.aps.org/doi/10.1103/PhysRevLett.67.2339.

[35] C.G. Van de Walle, D.B. Laks, G.F. Neumark, S.T. Pantelides, First-principles calculations of solubilities and doping limits: Li, na, and n in znse, Phys. Rev. B 47 (1993) 9425–9434, http://dx.doi.org/10.1103/PhysRevB.47.9425, URL https://link.aps.org/doi/10.1103/PhysRevB.47.9425.

[36] M. Leslie, N.J. Gillan, The energy and elastic dipole tensor of defects in ionic crystals calculated by the supercell method, J. Phys. C 18 (5) (1985) 973, http://dx.doi.org/10.1088/0022-3719/18/5/005, URL http://dx.doi.org/10.1088/0022-3719/18/5/005.

[37] G. Makov, M.C. Payne, Periodic boundary conditions in ab initio calculations, Phys. Rev. B 51 (1995) 4014–4022, http://dx.doi.org/10.1103/PhysRevB.51.4014, URL https://link.aps.org/doi/10.1103/PhysRevB.51.4014.

[38] C. Freysoldt, J. Neugebauer, C.G.V. d. Walle, Electrostatic interactions between charged defects in supercells, Phys. Status Solidi (B) 248 (5) (2011) 1067–1076, http://dx.doi.org/10.1002/pssb.201046289, URL https://onlinelibrary.wiley.com/doi/abs/10.1002/pssb.201046289.

[39] C. Freysoldt, J. Neugebauer, C.G. Van de Walle, Fully ab initio finite-size corrections for charged-defect supercell calculations, Phys. Rev. Lett. 102 (1) (2009) 016402, http://dx.doi.org/10.1103/PhysRevLett.102.016402, URL https://link.aps.org/doi/10.1103/PhysRevLett.102.016402.

[40] W.C. Dunlap, R.L. Watters, Direct measurement of the dielectric constants of silicon and germanium, Phys. Rev. 92 (1953) 1396–1397, http://dx.doi.org/10.1103/PhysRev.92.1396, URL https://link.aps.org/doi/10.1103/PhysRev.92.1396.

[41] V. Pelenitsyn, P. Korotaev, First-principles study of radiation defects in silicon, Comput. Mater. Sci. 207 (2022) 111273, http://dx.doi.org/10.1016/j.commatsci.2022.111273, URL https://www.sciencedirect.com/science/article/pii/S092702562200074X.

[42] A. Alkauskas, Q. Yan, C.G. Van de Walle, First-principles theory of nonradiative carrier capture via multiphonon emission, Phys. Rev. B 90 (2014) 075202, http://dx.doi.org/10.1103/PhysRevB.90.075202.

[43] M.E. Turiansky, A. Alkauskas, M. Engel, G. Kresse, D. Wickramaratne, J.-X. Shen, C.E. Dreyer, C.G. Van de Walle, Nonrad: Computing nonradiative capture coefficients from first principles, Comput. Phys. Comm. 267 (2021) 108056, http://dx.doi.org/10.1016/j.cpc.2021.108056.

[44] S. Kim, S.N. Hood, A. Walsh, Anharmonic lattice relaxation during nonradiative carrier capture, Phys. Rev. B 100 (2019) 041202, http://dx.doi.org/10.1103/PhysRevB.100.041202.

[45] D. Neamen, Semiconductor Physics and Devices, third ed., McGraw-Hill, Inc., USA, 2002.

[46] S. Kim, S.N. Hood, P. van Gerwen, L.D. Whalley, A. Walsh, Carriercapture.Jl: Anharmonic Carrier Capture, 2020, URL http://dx.doi.org/10.5281/zenodo.3707592.

[47] G. Henkelman, B.P. Uberuaga, H. Jónsson, A climbing image nudged elastic band method for finding saddle points and minimum energy paths, J. Chem. Phys. 113 (22) (2000) 9901–9904, arXiv:https://doi.org/10.1063/1.1329672 URL http://dx.doi.org/10.1063/1.1329672.

[48] G. Herrero-Saboya, L. Martin-Samos, A. Jay, A. Hemeryck, N. Richard, A comprehensive theoretical picture of E centers in silicon: From optical properties to vacancy-mediated dopant diffusion, J. Appl. Phys. 127 (8) (2020) 085703, URL http://dx.doi.org/10.1063/1.5140724.

[49] J. Dabrowski, G. Kissinger, Supercell-size convergence of formation energies and gap levels of vacancy complexes in crystalline silicon in density functional theory calculations, Phys. Rev. B 92 (14) (2015) 144104, http://dx.doi.org/10.1103/PhysRevB.92.144104, URL https://link.aps.org/doi/10.1103/PhysRevB.92.144104. publisher: American Physical Society.

[50] L. Shi, K. Xu, L.-W. Wang, Comparative study of ab initio nonradiative recombination rate calculations under different formalisms, Phys. Rev. B 91 (2015) 205315, http://dx.doi.org/10.1103/PhysRevB.91.205315, URL https://link.aps.org/doi/10.1103/PhysRevB.91.205315.

[51] O. Lui, P. Migliorato, A new generation–recombination model for device simulation including the poole-frenkel effect and phonon-assisted tunnelling, Solid-State Electron. 41 (4) (1997) 575–583, http://dx.doi.org/10.1016/S0038-1101(96)00148-7, URL https://www.sciencedirect.com/science/article/pii/S0038110196001487.

[52] W. Shockley, W.T. Read, Statistics of the recombinations of holes and electrons, Phys. Rev. 87 (1952) 835–842, http://dx.doi.org/10.1103/PhysRev.87.835, URL https://link.aps.org/doi/10.1103/PhysRev.87.835.

[53] R.N. Hall, Electron–hole recombination in germanium, Phys. Rev. 87 (1952) 387, http://dx.doi.org/10.1103/PhysRev.87.387, URL https://link.aps.org/doi/10.1103/PhysRev.87.387.

[54] A. Junkes, Influence of Radiation Induced Defect Clusters on Silicon Particle Detectors (Ph.D. thesis), Hamburg U, 2011.

[55] D. Passeri, P. Ciampolini, G. Bilei, F. Moscatelli, Comprehensive modeling of bulk-damage effects in silicon radiation detectors, IEEE Trans. Nucl. Sci. 48 (5) (2001) 1688–1693, http://dx.doi.org/10.1109/23.960358.

[56] M. Petasecca, F. Moscatelli, D. Passeri, G. Pignatel, C. Scarpello, Numerical simulation of radiation damage effects in p-type silicon detectors, Nucl. Instrum. Methods Phys. Res. A 563 (1) (2006) 192–195, http://dx.doi.org/10.1016/j.nima.2006.01.093, proceedings of the 7th International Workshop on Radiation Imaging Detectors. URL https://www.sciencedirect.com/science/article/pii/S0168900206002166.